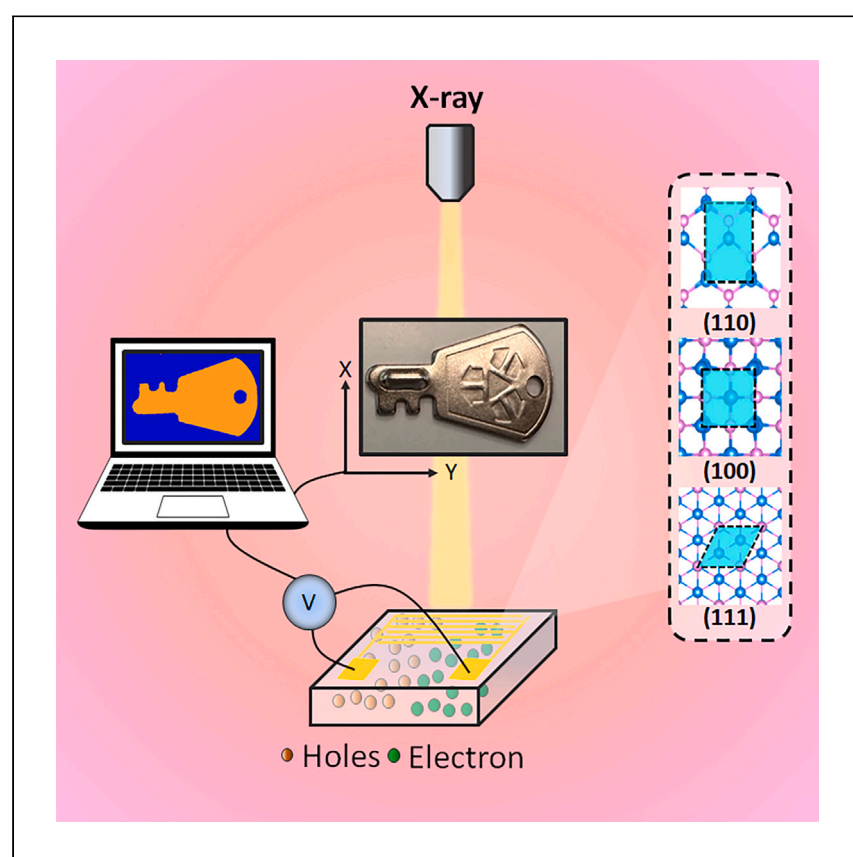**Article**

Crystallographic orientation-dependent photo-response of planar cadmium telluride X-ray detectors

Wang et al. demonstrate an alternative solution to optimize the X-ray detector performance by selecting crystals with appropriate crystallographic plane orientations. It can be carefully selected to meet the requirements of different real-life application scenarios under high or low electric fields.

Lijie Wang, Razan Nughays, Xin Song, ..., Jun Yin, Osman M. Bakr, Omar F. Mohammed

jun.yin@polyu.edu.hk (J.Y.)
osman.bakr@kaust.edu.sa (O.M.B.)
omar.abdelsaboor@kaust.edu.sa (O.F.M.)

Highlights

The impact of crystallographic orientation of cadmium telluride X-ray detectors is studied

Four-dimensional SEM to directly probe the transport of photo-induced charge carriers

(110)-plane cadmium telluride X-ray detector exhibits better performance than (100) or (111)

Appropriate cadmium telluride crystal orientations for different application scenarios

Article

Crystallographic orientation-dependent photo-response of planar cadmium telluride X-ray detectors

Lijie Wang,[1,5] Razan Nughays,[1,5] Xin Song,[2,5] Tieyuan Bian,[3] Mohamed Nejib Hedhili,[4] Jun Yin,[3,*] Osman M. Bakr,[2,*] and Omar F. Mohammed[1,2,6,*]

SUMMARY

Cadmium telluride (CdTe) crystals are widely used for X-ray detection in applications ranging from medical imaging to non-destructive industrial inspection. The surface charge carrier dynamics and photo-response of the crystals are critical factors that determine their per8formance. Here, we reveal the influence of crystallographic orientation of CdTe crystals on their photo-induced behaviors. Notably, X-ray detector devices fabricated from the (110) lattice plane exhibit more than two-orders of magnitude lower X-ray detection limit and a substantially higher X-ray sensitivity over the devices fabricated from either (100) or (111) crystal planes when subjected to a bias of 0.1 V. These findings are elucidated through comprehensive investigations by time-resolved spectroscopic and four-dimensional electron microscopic experiments, further supported by high-level density functional theory calculations. This discovery highlights the pivotal role of selecting an appropriate crystallographic orientation in enhancing the detection performance of high-energy X-ray sensors, thereby benefiting various X-ray imaging applications.

INTRODUCTION

The detection of high-energy radiation, such as X-rays, plays a critical role in various fields that have a substantial impact on our daily lives, including medical diagnosis,[1,2] computed tomography,[3,4] non-destructive inspection,[5] security,[6] and industrial monitoring.[7] X-ray imaging operates on two fundamental principles: indirect conversion of X-ray photons into low-energy optical photons in X-ray imaging scintillators or direct conversion of photons into electrical charges in X-ray detectors.[8,9] Key metrics for a direct conversion detector encompass the detection limit, characterized by a high-current signal generation coupled with low noise and X-ray sensitivity, denoting the detector's exceptional capability to not only respond to a specific radiation level but also to exhibit spatial resolution enabling high-quality imaging with minimal X-ray dose.[8]

Cadmium telluride (CdTe) has emerged as a highly promising material for X-ray detectors due to its large atomic number and high density, resulting in strong absorption and high detection efficiency of high-energy photons in the 10–140 keV range. In addition, the unique optical and transport features of CdTe, including high resistance and low leakage current, make it an ideal choice for a wide range of flat-panel imaging applications.[10–12] Moreover, CdTe crystal exhibits significant charge carrier mobility (μ) and long lifetime (τ), crucial for mitigating carrier trapping, recombination, and signal pulse amplitude degradation in X-ray detectors. This enables efficient charge transport in devices

with thicknesses spanning from millimeters (mm) to even centimeters (cm) when depletion occurs. However, the prevalent CdTe crystals grown using methods such as the traveling heater method and Bridgman techniques typically yield (111)-plane single crystals. The current research centers around the (111) orientation and often focuses on introducing or comparing crystal preparation methods or analyzing modifications in fundamental material properties following the incorporation of specific elements.[11,13,14] Although these crystals have good stability performance under high electric field and are widely used in industrial applications, they exhibit noticeable current fluctuations during X-ray detection testing and suffer from low hole transport that negatively impacts the detection limit and sensitivity,[12,15] and a comprehensive analysis of the underlying causes and potential alternative solutions is yet to be undertaken.

Crystallographic orientation, representing the arrangement of atoms within a crystal lattice, significantly influences the electronic and transport properties of materials.[16] In the context of CdTe, the structural properties critically govern the uniformity of charge transport, which determines the collection efficiency of free carriers induced by high-energy photons and noise sources within crystals. In this study, we conducted a systematic investigation on the impact of lattice plane orientation, specifically (110), (100), and (111), in CdTe crystals used for X-ray detectors in imaging applications. We combined ultrafast optical spectroscopy and four-dimensional ultrafast scanning electron microscopy (4D-USEM)[17,18] to directly probe the evolution and transport of photo-induced charge carriers on ultrafast timescales.[19–21] X-ray detection experiments were performed using X-ray detector devices based on these crystals with different plane orientations. The results demonstrated that CdTe X-ray detector devices fabricated from the (110) lattice plane exhibited a more than two orders of magnitude lower X-ray detection limit compared to devices fabricated from either (100) or (111) crystal planes. Furthermore, devices oriented along the (110) plane showed significantly higher X-ray sensitivity, surpassing that of commercially dominant α-Se and α-Si X-ray detectors by approximately 150-fold and 390-fold, respectively. These findings were consistent with the observed behaviors of photo-induced charge carrier lifetime and transport distances. Density functional theory (DFT) calculations attributed this phenomenon to higher charge carrier mobility and less electron scattering. Therefore, it highlights the importance of selecting appropriate CdTe crystallographic orientations to achieve enhanced resolution and sensitivity in flat-panel X-ray imaging applications, with particular relevance to the field of medical examinations and security inspections.

RESULTS AND DISCUSSION

Sample preparation and optical characterization

CdTe crystals with three different plane orientations, namely (110), (100), and (111), were investigated in this study. Detailed information about the samples and experimental methods can be found in the experimental procedures section and supplemental information. Before starting any experiments, the crystal surfaces were subjected to Ar ion sputtering for meticulous cleaning, ensuring the elimination of impurities and oxide layers. The X-ray diffraction pattern presented in Figure S1 confirmed the presence of the three crystalline structures, and the X-ray photoelectron spectra (XPS) depicted in Figure S2 demonstrated the successful elimination of oxygen, carbon, and other elements in all three samples after the etching process. Specifically, Figure S3 showcased high-resolution XPS spectra of Te 3d core level, revealing the presence of two distinct Te $3d_{3/2}$ components at 572.3 eV and 575.8 eV, corresponding to the Te^{2-} and Te^{4+} states, respectively, before the cleaning procedure.[22,23] However,
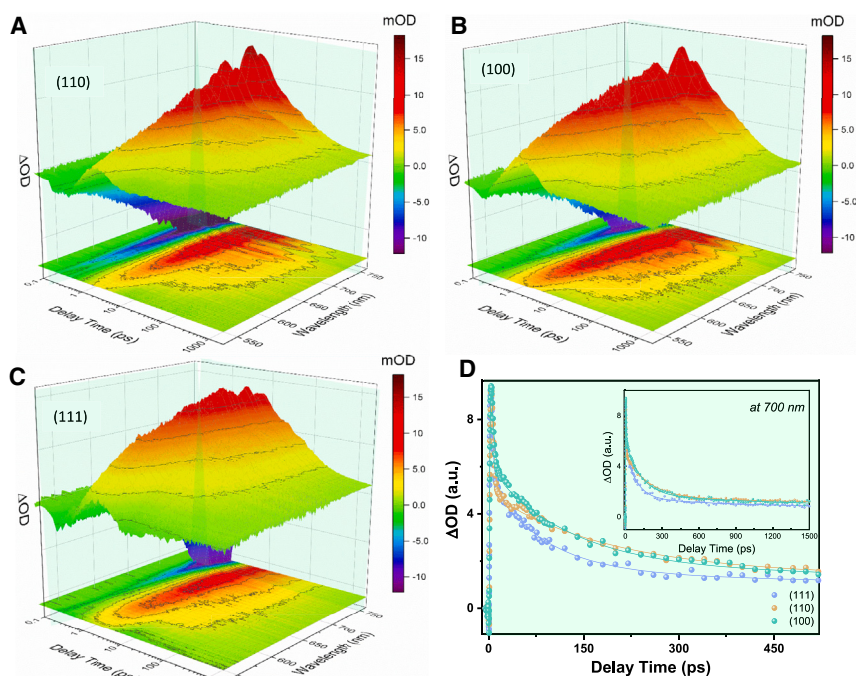
Figure 1. The transient spectroscopic results of CdTe crystals

(A–C) The time-wavelength-intensity 3D maps of (110), (100), and (111) CdTe crystals, obtained by exciting the sample with 400 nm under identical experimental conditions; the lower panel represents the corresponding 2D time-wavelength maps.

(D) Time traces of the three crystals obtained by probing them at 700 nm, along with fittings. The inset shows zoomed-out temporal traces until 1,500 ps.

the oxidation state (Te^{4+}) was completely eradicated following the surface etching treatment.

We performed transient optical spectroscopic studies on the three CdTe crystals to investigate the behavior of photo-induced charge carriers. The transient maps obtained through visible probing of the samples are illustrated in Figures 1A–1C, with the lower panels showcasing the projected time-wavelength maps. It is noteworthy that although the spectral features appear similar, the complete photo-cycle in (110) and (100) crystals exhibits a longer duration compared to that observed in the (111) crystal orientation. Figure 1D presents the time traces probed at 700 nm (1.77 eV) under 400-nm excitation, with green, orange, and purple dots representing the experimental traces, and solid lines indicating their fits. The three kinetic traces have been normalized at the maximum signal and are displayed within a time delay of 500 ps. Additional traces with longer (1,500 ps) and shorter (100 ps) time windows are shown in the inset and Figure S4, respectively. Following photoexcitation, the transient reflectivity (TR) signals for all three crystals initially exhibit a negative sign but transition to positive within approximately 5 ps. Subsequently, they undergo rapid decay with time constants of 4.16 ps for (110), 4.44 ps for (100), and 3.35 ps for (111) plane orientations. In the long-time component, the decay dynamics differ significantly: the (111) orientation exhibits the quickest decay (τ_2: 85.9 ps, τ_3: 899.4 ps) compared to slower decays in (110) (τ_2: 126.6 ps, τ_3: 1.65 ns) and (100) (τ_2: 185.6 ps, τ_3: 1.49 ns). The first two lifetime components have been attributed to electron trapping by the shallow and deep trap states,[24,25] respectively, while the longer one is likely due to laser-induced heating.[26] These observations imply a faster recombination of photo-induced electron-hole pairs in (111) crystals compared to (110) and (100) crystals.
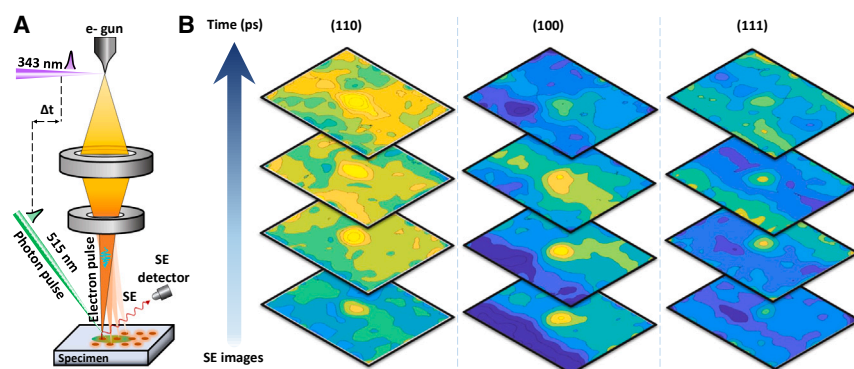
Figure 2. Photo-induced charge carrier transport behaviors obtained by 4D-USEM

(A) A schematic diagram of 4D-USEM. In this configuration, electron pulses are generated through the utilization of a 343-nm pulsed laser beam, serving as the probing source, while a 515-nm beam (green) acts as a pump beam to initiate the dynamic processes. The signal is collected by employing a secondary electron (SE) detector.

(B) The color-coded USEM images for (110)-, (100)-, and (111)-oriented crystal obtained as a function of delay time.

Photo-induced surface charge carrier dynamics

The transport characteristics of photo-induced charge carriers on the crystal surface were investigated using 4D-USEM. In this experiment, a beam of pulsed electrons was generated from the SEM's gun source by focusing a 343-nm probing beam on it. Another 515-nm beam was used to excite the surface of the sample and to generate electron-hole pairs,[27,28] as depicted in Figure 2A. The time-resolved secondary electron (SE) images were acquired by subtracting the excited signals from the unexcited (at negative time delays) ones. No signal was observed at large negative delay times (e.g., −450 ps), indicating the complete restoration of the specimen to its initial equilibrium state prior to the subsequent stroboscopic probing event (see Figure S5 and Note S1).[29] Figure 2B presents representative color-coded diffusion patterns of charge carriers on the three samples. The images were fitted with a 2D Gaussian function to improve the signal-to-noise ratio and provide qualitative information regarding the carrier transport behaviors of CdTe crystals at different delay times for three distinct orientations. Figure S6 displays the charge carrier diffusion, wherein the dashed white lines represent the reference positions of the pump-induced spots across all images. The transport distances of the three samples were measured over a range of approximately 11–220 ps, offering insights into the spreading and diffusion extent of the charge carriers, as shown in Figure S7. Notably, the (110)-plane sample exhibited the longest diffusion length of 15.5 μm, followed by the (100)-plane crystal with a comparable diffusion length of 13.2 μm. In contrast, the (111)-plane crystal demonstrated a shorter diffusion distance of 9.5 μm, indicating a superior surface carrier transport performance in the (110) and (100) crystals compared to the (111) crystals (see also Figure S8). These results align well with the TR measurements. Given that the three crystals were grown under identical conditions and underwent pre-cleaning before measurements, the observed differences can be attributed solely to variations in inhomogeneity of the surface morphology, roughness, and the surface's physical and transport properties arising from the distinct lattice plane orientations.

DFT calculations

We further performed DFT calculations to provide insights into the transient behaviors of photo-induced charge carriers in different plane orientations of CdTe crystals. Figures 3A–3C present the optimized slab structures of (110)-, (100)-, and (111)-plane
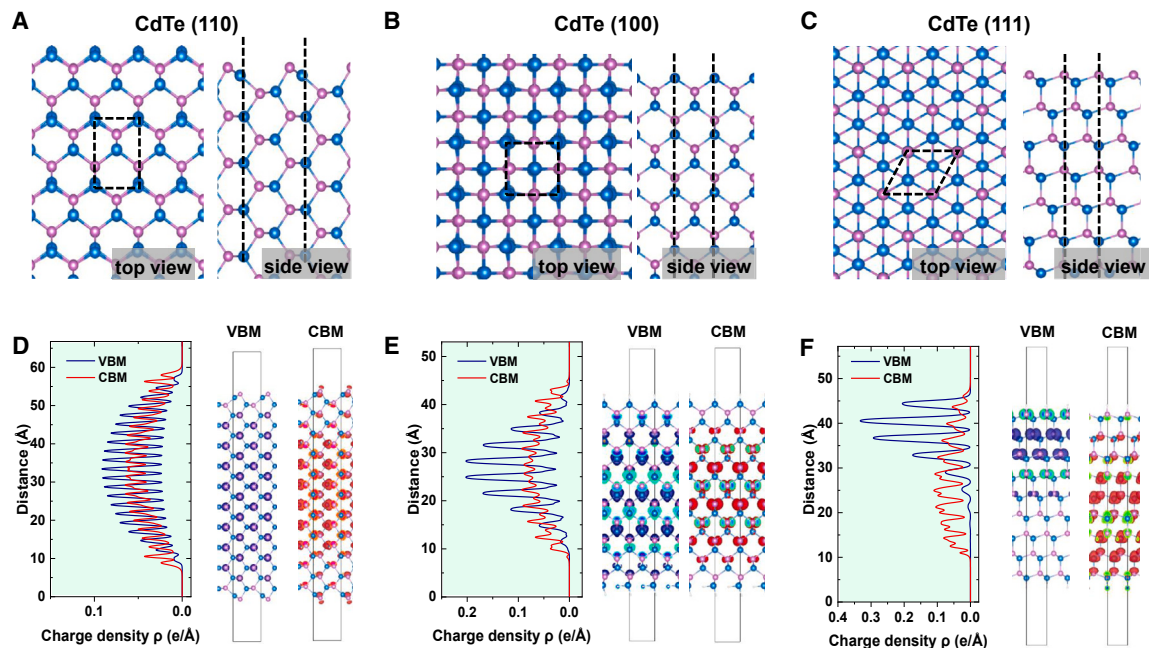
Figure 3. The DFT calculations on the three CdTe crystals

(A–C) Top and side views of the optimized slab structures for CdTe (110), (100), (111) plane orientations, respectively. Cd atoms are blue, Te atoms are pink, surface H-terminations are omitted, and the black dashed lines indicate the slab cells for DFT calculations.

(D–F) Three-dimensional charge densities for VBM and CBM of CdTe (110), (100), and (111) plane orientations, respectively.

CdTe crystals, both in top and side views, with black dashed lines indicating the slab cells used for DFT calculations. It is noteworthy that the effective current flow directions are orthogonal to the studied plane orientations on the top surface, in alignment with the experiments. CdTe is zincblende crystal with a sphalerite structure, crystallizing in the cubic space group.[30,31] In this structure, Cd^{2+} is bonded to four equivalent Te^{2-} atoms, forming a corner-sharing $CdTe_4$ tetrahedral, while Te^{2-} is bonded to four equivalent Cd^{2+} atoms, forming a corner-sharing $TeCd_4$ tetrahedral, and all Cd–Te bond lengths are 2.84 Å. The (110)-plane crystal exhibits a triangular channel-row structure, while the (100) crystal surface consists of square islands with a close-packed tetrahedral arrangement. In the (111)-plane orientation, the Cd atoms form a hexagonal shape on the top layer. Figures 3D–3F illustrate the three-dimensional charge densities for valence band maximum (VBM) and conduction band minimum (CBM) of CdTe. The charge density distribution in the (110) and (100) crystals is delocalized, whereas in the (111) crystal, it is more localized, with the VBM predominantly distributed at the top (see also Figure S9). The effective mass describes the behavior of an electron within a crystal lattice under an external electric field. It represents the inertia of the electron in the crystal lattice and is related to the curvature of the electron energy bands in the material. In the (110)-plane CdTe crystal, the effective mass is reduced to 0.079 m_0, indicating higher carrier mobility and larger transport speed compared to the other two crystals, as shown in Figure S10A. The values are similar in the (100)- and (111)-plane crystals, although the latter is slighter larger. Figure S10B shows the electron density of the CdTe crystals with different plane orientations, and the surface electron density of (111)-plane crystal is approximately 3 and 1.4 times higher than that of the (110)- and (100)-plane crystals, respectively. This suggests a higher electron packing density in the (111) crystal, leading to a higher probability of electron-electron interactions.[16] Consequently, the electrostatic repulsion between electrons is expected to be stronger in the (111) crystal, resulting in shorter carrier diffusion compared to the (110) and (100) crystals. The resulting
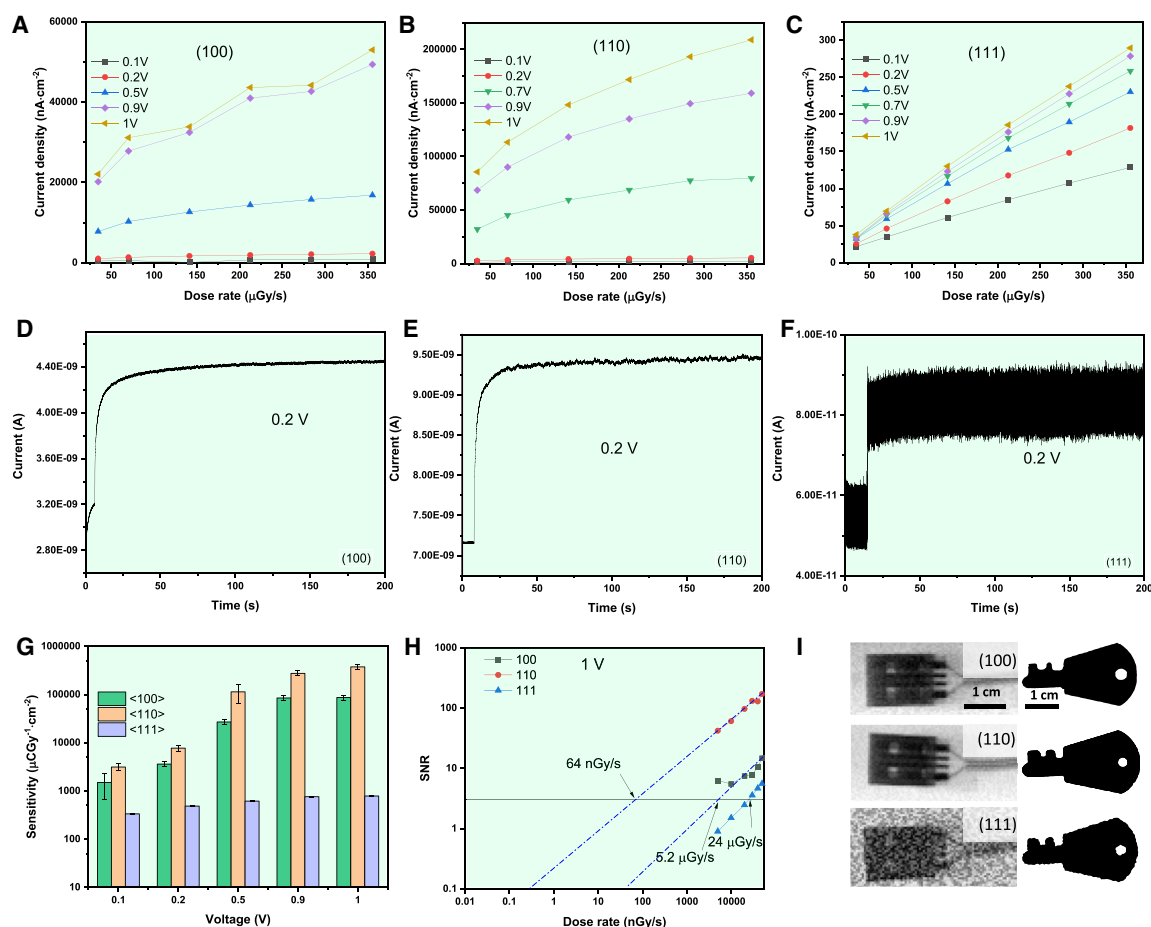
Figure 4. The performance of CdTe X-ray detectors

(A–C) The relationship between X-ray photocurrent and dose rate (34–355 µGy s^{-1}) under different bias voltages for different plane orientations of (110), (100), and (111).

(D–F) Photocurrent stability measurement of CdTe crystals with different plane orientations under continuous X-ray irradiation with a constant 0.2 V bias.

(G) X-ray sensitivities of different devices in the bias range of 0.1–1 V. The detection limit was obtained by the epitaxy method and was derived from the slope of the fitting lines from (A), (B), and (C). The error bars represent the deviation of the slope in the fitting process.

(H) Signal-to-noise ratio (SNR) of the three devices with different CdTe plane orientations as a function of dose rate.

(I) X-ray images of a USB port and a metal key taken by the (110) (up), (100) (mid), and (111) (bottom) detectors at a dose rate of 550 µGy s^{-1}. The real photos of the USB port and metal key can be found in Figure S13. Scale bars represent 1 cm.

trade-off between effective mass and density indicates that the (110)-plane crystal exhibits the most favorable overall behavior among the three plane orientations of CdTe crystals.

X-ray detection performance

To assess the photo-response of the CdTe crystal samples under X-ray excitation, we fabricated planar X-ray detector devices with three different plane orientations. Figure S11 provides a schematic illustration of the device structure. Interdigitated gold electrodes were thermally evaporated onto the crystal surface immediately after surface etching by Ar ion sputtering, and an electric field was applied during measurements. Under X-ray radiation and with the application of bias, the movement of electrons and holes generates a response current in the detector. We compared the photocurrent densities as a function of dose rates in the bias range of 0.1–1 V for the (110)-, (100)-, and (111)-plane devices (Figures 4A–4C). All three devices exhibited a linear increase in photocurrent

density with increasing dose rates (34–355 μGy s^{-1}). However, the linear trend of the (100)-plane device became fluctuant when the bias voltage exceeded 0.5 V, likely due to current fluctuations during the test. In contrast, this phenomenon was nearly absent in the (110)- and (111)-plane devices, indicating relatively stable current within this high voltage range, especially for the (111)-plane devices. Furthermore, we observed a significantly higher increase in current density for the (110)-plane device compared to the other two, suggesting its potential for higher sensitivity and current response. To evaluate device stability, we measured the current stability of the devices in ambient conditions for 200 s with different plane orientations at a dose rate of 31 μGy s^{-1} and a bias voltage of 0.2 V (Figures 4D–4F). The (100)-plane device exhibited a certain drift in both dark current and photocurrent, whereas the (110)- and (111)-plane devices did not show this undesirable phenomenon.

Based on the current densities presented in Figures 4A–4C, we have calculated the sensitivity of the three CdTe devices across a dose range of 34–355 μGy s^{-1}, as shown in Figure 4G. The (100)- and (111)-plane devices exhibited sensitivities of 1,497 and 334 μC Gy·cm^{-2} at a bias of 0.1 V, respectively, while the (110)-plane device demonstrated significantly higher sensitivity at 3,127 μC Gy·cm^{-2}, surpassing the sensitivities of commercially dominant α-Se and α-Si X-ray detectors,[10,32,33] which typically range around 20 and 8 μC Gy·cm^{-2}, respectively. At a bias of 1 V, the sensitivities further increased to 374,383, 86,574, and 784 μC Gy·cm^{-2} for the (110)-, (100)-, and (111)-plane devices, respectively. These sensitivity values, particularly for the (110)-plane CdTe detector, far exceed the reported sensitivities of perovskite-based X-ray detectors, which usually fall within the range of 10^3-10^4 μC Gy·cm^{-2}.[34,35] Furthermore, the signal-to-noise ratios (SNR) of the devices were influenced by their lattice plane orientations, as depicted in Figure 4H, with the (110)-plane device exhibiting the highest SNR. The detection limit, another crucial metric of detector performance, was determined from the SNR figure using the epitaxy method. The (110)-plane device displayed the lowest detection limit value of 64 nGy s^{-1} at 1 V, while the (100)- and (111)-plane devices had detection limits of 5.2 μGy s^{-1} and 24 μGy s^{-1} at the same bias, respectively. These values for the (110)-plane and (100)-plane CdTe devices are lower than those of regular medical diagnostics based on active personal dosimeters, which typically have a detection limit of 5.5 μGy s^{-1}.[36,37] Nevertheless, the (111)-plane device can also achieve a better detection limit by increasing the applied voltage, given its super stability performance under high electric field.[10] From all of the above, it is evident that the (110)-plane CdTe device exhibits the highest sensitivity and the lowest detection limit, making it the most suitable plane orientation for low-dose X-ray radiation detection under low bias voltage.

X-ray imaging

To compare the imaging performance of the three CdTe X-ray detector devices, we conducted a low-dose single-pixel imaging experiment using a moving x-y stage to record the electrical signal of the detector. The experiment was conducted at a fixed position with a scanning step of 0.5 mm and a scanning speed of 0.5 mm s^{-1}, and the collected current was used to generate the image. The experiment was carried out at dose rates of 10 and 550 μGy s^{-1} under a bias of 0.2 V. A schematic diagram of the imaging device structure is shown in Figure S12, and the resulting images for the three plane devices under 550 μGy s^{-1} are presented in Figure 4I for a USB port and a metal key (Figure S13). Both the (110)- and (100)-plane devices enable clear visualization of the internal structure beneath the USB's black rubber, and it was particularly pronounced on the (110)-plane devices, where traces of the rubber were discernible. In contrast, the (111)-plane device only facilitates rudimentary

contour recognition, with significant distortion in the detailed region. Furthermore, the (110)-plane device produced a highly resolved and undistorted image of a metal key without any current drift, and the (100)-plane device also produced a clear image with only minor distortion at the edge of the key under the same dose rate, while the (111)-plane device exhibited insufficient resolution, particularly at the key's edge, and experienced some current drift. When the dose was reduced to 10 μGy s^{-1} (Figure S14), the (111)-plane device could hardly recognize any image signal, whereas the (110)-plane device still produced a high-definition-resolution image. The (100)-plane device was able to distinguish the image, but the resolution dropped dramatically compared to the (110)-plane device (Figure S14B). These results indicate that the sensitivity and detection limits of the CdTe devices have a significant impact on the imaging resolution, with the (110)-plane device demonstrating the best performance, followed by the (100)- and the (111)-plane devices.

In summary, we fabricated planar X-ray detector devices using CdTe crystals with three different lattice plane orientations. Our investigations demonstrate that the (110)-plane device exhibits superior X-ray detection performance particularly for low-dose X-ray radiation detection under low bias voltage, outperforming not only (100)- and (111)-plane devices but also exceeding commercial X-ray detectors. More specifically, the (110) lattice plane device exhibited exceptional X-ray detection capabilities, with a remarkably low detection limit of 64 nGy s^{-1} at 1 V, nearly 85 times lower than the dosage typically required for a standard medical examination. Furthermore, the (110)-plane devices show X-ray sensitivity surpassing those of commercially dominant α-Se and α-Si detectors,[10,32,33] as well as widely reported perovskite-based X-ray detectors.[34,35] These results are in line with the transient spectroscopic and microscopic behaviors observed in the three CdTe single crystals and are supported by DFT calculations. Therefore, this discovery provides an alternative solution to optimize the detector performance by selecting crystals with appropriate crystallographic plane orientations to meet the requirements of different application scenarios under high and low electric fields, with profound implications for various real-life application scenarios and potential extensions to other material systems utilized in X-ray detectors.

EXPERIMENTAL PROCEDURES

Resource availability

Lead contact
Further information and requests for resources and reagents should be directed to, and will be fulfilled by, the lead contact, Omar F. Mohammed (omar.abdelsaboor@kaust.edu.sa).

Materials availability
This study did not generate new unique reagents.

Data and code availability
All data needed to evaluate the conclusions in the paper are present in the main text or the supplemental information and are available upon reasonable request from the lead contact.

Materials
CdTe single crystals with the three lattice plane orientations, (110), (100), and (111), were purchased from MTI Corporation (Materials Tech. Intl., USA). The crystals were undoped, p-type, and 5 mm × 5 mm in area. The crystals have no ligands on top, and no treatment has been done except removing the oxide layers by using the Ar ion

sputtering process. XPS was employed before and after surface etching to examine the elimination of impurities. The XPS measurements were carried out in a Kratos Axis Supra DLD spectrometer (hν = 1,486.6 eV) operating at 75 W, a multichannel plate, and delay line detector under a vacuum of 1×10^{-9} mbar equipped with a monochromatic Al K X-ray source. Survey and high-resolution spectra were performed at fixed analyzer pass energies of 160 and 20 eV, respectively. The etching process was performed using Ar^+ ion beam etching operated at 5 keV.

Transient spectroscopic measurements

The broadband visible TR measurements were performed using a Helios pump-probe setup (Ultrafast Systems), which allowed a tunable visible excitation of the samples. A 1-kHz 800-nm ~150 fs/7 mJ laser pulse was split into two parts for the pump and probe. The pump was obtained using a nonlinear optical parametric amplifier (SpectraPhysics), which delivered pulses in the visible, and the probe was generated by focusing the rest of the 800-nm beam into a 2-mm CaF_2 crystal. Particularly, the white-light probe beam was further split into two beams; one was used as a reference to reduce the SNR significantly. The pump and electronically delayed probe were then spatially overlapped on the sample, and the reflected signal was collected and focused into a fiber detector. The pump power used for the experiments is 150 μW with a repetition rate of 500 Hz, and the detailed experimental setup and analysis software of the Helios system can be found elsewhere.[38]

4D-USEM measurements

In this technique an infrared laser system is coupled with SEM. The infrared beam is divided into two beams and guided to a second harmonic generator and third harmonic generator to produce two beams with different wavelengths, 515 nm (pump beam) and 343 nm, directed to the gun source inside the microscope to create primary pulsed electrons through photoelectron effect. The primary pulsed electrons will be accelerated and focused by different magnetic lenses and then guided to the sample to probe the surface of the sample to generate SEs, while the pump beam will hit the sample's surface to initiate the dynamics. The arrival for pump beam is controlled by optical delay line to introduce an extra traveling distance to match the probe beam. The experiments were conducted using repetition rate of 8.33 MHz, with different powers for the pump beam ranging from 0.56, 0.25, and 0.20 mW for (110), (100), and (111) to avoid photo damage. For the SEM parameters, 30 kV accelerating voltage was applied, and the SEM images were obtained using 100-ns dwell time and 64 frames.

DFT calculations

We carried out DFT calculations using the projector-augmented wave method as implemented in the Vienna Ab initio Simulation Package code.[39,40] The generalized gradient approximation together with the Perdew-Burke-Ernzerhof exchange-correlation functional was used. A uniform grid of $6 \times 6 \times 6$ k-mesh in the Brillouin zone was employed to optimize the crystal structure of bulk CdTe, and $4 \times 4 \times 1$ k-mesh for CdTe slabs. The energy cutoffs of the wavefunctions were set at 500 eV for the bulk and slabs. The unit cells had a (1×1) lateral periodicity and contained 20 octahedral layers of CdTe with exposed (110), (100), and (111) surfaces. All the symmetric slabs were put in the middle of crystal structures separated by both top and bottom vacuum layers (~10 Å) to prevent spurious interslab interactions. Each structure was optimized until forces on single atoms were smaller than 0.01 eV/Å.

X-ray detection and X-ray imaging

Interdigitated Au electrodes were deposited on the surface of the single crystals by vacuum evaporation to fabricate the planar photodetectors. The spacing between neighboring fingers was 40 μm, and the effective illuminated area of each device was approximately 2×10^{-3} cm^2. The X-ray-related measurements and images were recorded using a 2-mm-thick, Al-filtered, tungsten anode source and operated with a constant 40 kV voltage, resulting in a dose range of 34–355 μGy$_{air}$·s^{-1} by varying the magnitude of the tube current. A RaySafe X2 MAM Sensor was used to calibrate the X-ray dose rate. The X-ray response of the devices was obtained using a Keysight B2902A semiconductor characterization system and a manual probe station under various bias voltages. The X-ray peak energy was estimated to be 29 keV by using the software (SPEKTR3.0), which was kindly shared by the I-STAR lab at Johns Hopkins University and can be freely downloaded from http://istar.jhu.edu/downloads/. The CdTe X-ray detectors were characterized by moving the imaging targets in the horizontal x-y direction and collecting the electrical signals in a fixed position; thus, the attenuated X-rays were detected by the CdTe detectors.

Calculation of signal-to-noise ratio

The noise current was determined by calculating the standard deviation of the photocurrent to obtain the SNR. The detection limit is defined by the IUPAC standard as the equivalent dose rate to produce a signal greater than three times the noise level, so we used the dose rate with an SNR value of 3 as the detection limit at a given electric field.

The signal current (I_s) was derived by subtracting the average dark current (I_d) from the average photocurrent (I_p). The noise current (I_n) was obtained by calculating the standard deviation of the photocurrent.

$$I_{signal} = \bar{I}_P - \bar{I}_d \qquad \text{(Equation 1)}$$

$$I_{noise} = \sqrt{\frac{1}{N}\sum_{i}^{N}\left(I_i - \bar{I}_p\right)^2} \qquad \text{(Equation 2)}$$

Then the SNR was calculated according to the following equation:

$$SNR = \frac{I_{signal}}{I_{noise}} \qquad \text{(Equation 3)}$$

SUPPLEMENTAL INFORMATION

ACKNOWLEDGMENTS

AUTHOR CONTRIBUTIONS

O.F.M. conceived the idea, L.W., R.N., and X.S. designed the overall experiments. J.Y., O.M.B., and O.F.M. co-supervised the project. L.W. and R.N. performed time-resolved spectroscopic and microscopic measurements, X.S. performed X-ray detection and imaging experiments, and T.B. performed calculations. M.N.H. performed the XPS experiment, and L.W., R.N., X.S., and O.F.M. contributed to the results analysis and interpretation. L.W., R.N., and X.S. wrote the manuscript. All authors contributed to the discussion of the results and reviewed the manuscript.

DECLARATION OF INTERESTS

The authors declare no competing interests.

REFERENCES

1. Zhou, S.-A., and Brahme, A. (2008). Development of phase-contrast X-ray imaging techniques and potential medical applications. Phys. Med. 24, 129–148.

2. Mould, R.F. (1995). The early history of x-ray diagnosis with emphasis on the contributions of physics 1895-1915. Phys. Med. Biol. 40, 1741–1787.

3. Withers, P.J., Bouman, C., Carmignato, S., Cnudde, V., Grimaldi, D., Hagen, C.K., Maire, E., Manley, M., Du Plessis, A., and Stock, S.R. (2021). X-ray computed tomography. Nat. Rev. Methods Primers 1, 18.

4. Kerckhofs, G., Schrooten, J., Van Cleynenbreugel, T., Lomov, S.V., and Wevers, M. (2008). Validation of x-ray microfocus computed tomography as an imaging tool for porous structures. Rev. Sci. Instrum. 79, 013711.

5. Hanke, R., Fuchs, T., and Uhlmann, N. (2008). X-ray based methods for non-destructive testing and material characterization. Nucl. Instrum. Methods Phys. Res. Sect. A Accel. Spectrom. Detect. Assoc. Equip. 591, 14–18.

6. Zentai, G. (2010). X-ray imaging for homeland security. Int. J. Signal Imag. Syst. Eng. 3, 13–20.

7. Martin, T., Koch, A., and Nikl, M. (2017). Scintillator materials for x-ray detectors and beam monitors. MRS Bull. 42, 451–457.

8. Zhou, Y., Chen, J., Bakr, O.M., and Mohammed, O.F. (2021). Metal halide perovskites for X-ray imaging scintillators and detectors. ACS Energy Lett. 6, 739–768.

9. Wu, H., Ge, Y., Niu, G., and Tang, J. (2021). Metal halide perovskites for X-ray detection and imaging. Matter 4, 144–163.

10. Eisen, Y., and Shor, A. (1998). CdTe and CdZnTe materials for room-temperature X-ray and gamma ray detectors. J. Cryst. Growth 184–185, 1302–1312.

11. Ruat, M., and Ponchut, C. (2012). Characterization of a pixelated CdTe X-ray detector using the Timepix photon-counting readout chip. IEEE Trans. Nucl. Sci. 59, 2392–2401.

12. Takahashi, T., and Watanabe, S. (2001). Recent progress in CdTe and CdZnTe detectors. IEEE Trans. Nucl. Sci. 48, 950–959.

13. Fiederle, M., Ebling, D., Eiche, C., Hofmann, D.M., Salk, M., Stadler, W., Benz, K.W., and Meyer, B.K. (1994). Comparison of CdTe, Cd0.9Zn0.1Te and CdTe0.9Se0.1 crystals: application for γ- and X-ray detectors. J. Cryst. Growth 138, 529–533.

14. Mycielski, A., Wardak, A., Kochanowska, D., Witkowska-Baran, M., Szot, M., Jakieła, R., Domagała, J.Z., Kowalczyk, L., Kochański, M., Janusz, G., et al. (2021). CdTe-based crystals with Mg, Se, or Mn as materials for X and gamma ray detectors: Selected physical properties. Prog. Cryst. Growth Char. Mater. 67, 100543.

15. Procz, S., Roque, G., Avila, C., Racedo, J., Rueda, R., Santos, I., and Fiederle, M. (2020). Investigation of CdTe, GaAs, Se and Si as sensor materials for mammography. IEEE Trans. Med. Imaging 39, 3766–3778.

16. El-Zohry, A.M., Shaheen, B.S., Burlakov, V.M., Yin, J., Hedhili, M.N., Shikin, S., Ooi, B., Bakr, O.M., and Mohammed, O.F. (2019). Extraordinary Carrier Diffusion on CdTe Surfaces Uncovered by 4D Electron Microscopy. Chem 5, 706–718.

17. Najafi, E., Scarborough, T.D., Tang, J., and Zewail, A. (2015). Four-dimensional imaging of carrier interface dynamics in pn junctions. Science 347, 164–167.

18. Chergui, M. (2015). Ultrafast photophysics of transition metal complexes. Acc. Chem. Res. 48, 801–808.

19. Nughays, R.O., Yang, C., Nematulloev, S., Yin, J., Harrison, G.T., Zhao, J., Fatayer, S., Bakr, O.M., and Mohammed, O.F. (2023). Visualization of Surface Charge Carrier Diffusion Lengths in Different Perovskite Crystal Orientations Using 4D Electron Imaging. Adv. Opt. Mater. 11, 2300190.

20. Zewail, A.H. (2010). Four-dimensional electron microscopy. Science 328, 187–193.

21. Strandell, D., Sonnichsen, C., and Kambhampati, P. (2022). Watching Excitations in CsPbBr3 Perovskite Nanocrystals Undergo Ultrafast Relaxation to Their Emitting State. J. Phys. Chem. C 126, 20505–20510.

22. Reese, M.O., Perkins, C.L., Burst, J.M., Farrell, S., Barnes, T.M., Johnston, S.W., Kuciauskas, D., Gessert, T.A., and Metzger, W.K. (2015). Intrinsic surface passivation of CdTe. J. Appl. Phys. 118, 155305.

23. Kowalski, B.J., Orłowski, B., and Ghijsen, J. (1998). XPS study of CdTe (110) surface oxidation process. Surf. Sci. 412–413, 544–554.

24. Burda, C., Link, S., Green, T.C., and El-Sayed, M.A. (1999). New transient absorption observed in the spectrum of colloidal CdSe nanoparticles pumped with high-power femtosecond pulses. J. Phys. Chem. B 103, 10775–10780.

25. Sekhar, M.C., and Samanta, A. (2015). Ultrafast Transient Absorption Study of the Nature of Interaction between Oppositely Charged Photoexcited CdTe Quantum Dots and Cresyl Violet. J. Phys. Chem. C 119, 15661–15668.

26. Zong, A., Kogar, A., Bie, Y.-Q., Rohwer, T., Lee, C., Baldini, E., Ergeçen, E., Yilmaz, M.B., Freelon, B., Sie, E.J., et al. (2019). Evidence for topological defects in a photoinduced phase transition. Nat. Phys. 15, 27–31.

27. Sun, J., Melnikov, V.A., Khan, J.I., and Mohammed, O.F. (2015). Real-Space Imaging of Carrier Dynamics of Materials Surfaces by Second-Generation Four-Dimensional Scanning Ultrafast Electron Microscopy. J. Phys. Chem. Lett. 6, 3884–3890.

28. Shaheen, B.S., El-Zohry, A.M., Zhao, J., Yin, J., Hedhili, M.N., Bakr, O.M., and Mohammed, O.F. (2020). Real-Space Mapping of Surface-Oxygen Defect States in Photovoltaic Materials Using Low-Voltage Scanning Ultrafast Electron Microscopy. ACS Appl. Mater. Interfaces 12, 7760–7767.

29. Mohammed, O.F., Yang, D.-S., Pal, S.K., and Zewail, A.H. (2011). 4D scanning ultrafast electron microscopy: visualization of materials surface dynamics. J. Am. Chem. Soc. 133, 7708–7711.

30. Balakhayeva, R., Akilbekov, A., Baimukhanov, Z., Giniyatova, S., Zdorovets, M., Gorin, Y., Popov, A.I., and Dauletbekova, A. (2020). Structure properties of CdTe nanocrystals created in SiO2/Si ion track templates. Surf. Coating. Technol. 401, 126269.

31. Yeremyan, A., Avetisyan, H., Avjyan, K., Vardanyan, G., and Khachatryan, A. (2008). Pulsed laser deposition of layers and nanostructures based on cadmium telluride and bismuth. Micro-and Nanoelectronics 7025, 213–218.

32. Tian, S., Sui, F., He, K., Cheng, G., Ge, Y., Ning, D., Wang, Z., Wang, Z., Tao, G., Wang, Z., et al. (2020). Co-axial silicon/perovskite heterojunction arrays for high-performance direct-conversion pixelated X-ray detectors. Nano Energy 78, 105335.

33. Guerra, M., Manso, M., Longelin, S., Pessanha, S., and Carvalho, M.L. (2012). Performance of three different Si X-ray detectors for portable XRF spectrometers in cultural heritage applications. J. Instrum. 7, C10004.

34. Su, Y., Ma, W., Yang, Y.M., and Michael). (2020). Perovskite semiconductors for direct X-ray detection and imaging. J. Semicond. 41, 051204.

35. Cui, Q., Song, X., Liu, Y., Xu, Z., Ye, H., Yang, Z., Zhao, K., and Liu, S.F. (2021). Halide-modulated self-assembly of metal-free perovskite single crystals for bio-friendly X-ray detection. Matter *4*, 2490–2507.

36. Song, X., Cui, Q., Liu, Y., Xu, Z., Cohen, H., Ma, C., Fan, Y., Zhang, Y., Ye, H., Peng, Z., et al. (2020). Metal-Free Halide Perovskite Single Crystals with Very Long Charge Lifetimes for Efficient X-ray Imaging. Adv. Mater. *32*, 2003353.

37. Eisen, Y., Shor, A., and Mardor, I. (2004). CdTe and CdZnTe X-ray and gamma-ray detectors for imaging systems. IEEE Trans. Nucl. Sci. *51*, 1191–1198.

38. El-Ballouli, A.O., Alarousu, E., Bernardi, M., Aly, S.M., Lagrow, A.P., Bakr, O.M., and Mohammed, O.F. (2014). Quantum Confinement-Tunable Ultrafast Charge Transfer at the PbS Quantum Dot and Phenyl-C61-butyric Acid Methyl Ester

Interface. J. Am. Chem. Soc. *136*, 6952–6959.

39. Kresse, G., and Hafner, J. (1993). Ab initio molecular dynamics for open-shell transition metals. Phys. Rev. B *48*, 13115–13118.

40. Kresse, G., and Furthmüller, J. (1996). Efficient iterative schemes for ab initio total-energy calculations using a plane-wave basis set. Physical review B *54*, 11169–11186.